Heterodyne Eddy Current Testing Using Magnetoresistive Sensors for Additive Manufacturing Purposes

Henrik Ehlers, Matthias Pelkner, and Roland Thewes, *Senior Member, IEEE*

***Abstract*—In recent years additive manufacturing technologies have become widely popular. For complex functional components or low volume production of workpieces, laser powder bed fusion can be used. High safety requirements, e.g. in the aerospace sector, demand extensive quality control. Therefore, offline non-destructive testing methods like computed tomography are used after manufacturing. Recently, for enhanced profitability and practicality online non-destructive testing methods, like optical tomography have been developed. This paper discusses the applicability of eddy current testing with magnetoresistive sensors for laser powder bed fusion parts. For this purpose, high spatial resolution giant magnetoresistance arrays are utilized for testing in combination with a single wire excitation coil. A heterodyne principle minimizes metrology efforts. This principle is compared to conventional signal processing in an eddy current testing setup using an aluminum test sample with artificial surface defects. To evaluate the influence of the powder used in the manufacturing process on eddy current testing and vice versa, a laser powder bed fusion mock-up made from stainless steel powder (316L) is used with artificial surface defects down to 100 μm. This laser powder bed fusion specimen was then examined using eddy current testing and the underlying principles.**

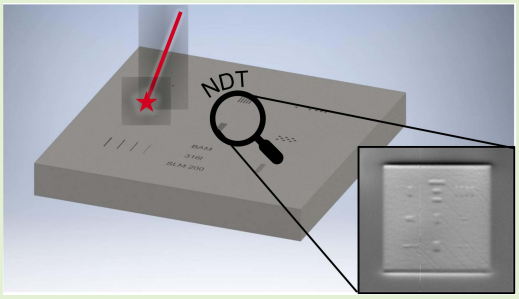

***Index Terms*— Eddy current testing, giant magnetoresistance, additive manufacturing, laser powder bed fusion, 316L, heterodyning.**

I. Introduction

COMPARED to conventional manufacturing techniques like milling, additive manufacturing (AM) enables production of relatively complex workpieces without wasting much material. Laser powder bed fusion (LPBF) represents an AM approach, which is nowadays common in industry. Here, metal parts with complex geometries are produced by melting subsequently layer after layer of powder with a laser retaining the properties of the base material [1]. This manufacturing process is not easy to control and slight differences in powder, temperature, speed, or other parameters can lead to a variety of defects in the processed material changing its mechanical properties and therefore decreasing its structural integrity [2], [3]. The manufactured parts are tested afterwards either with destructive testing methods to evaluate process and material parameters, or non-destructive testing (NDT) so that the workpiece can still be utilized after testing is completed.

There are approaches and systems integrating NDT methods into LPBF setups for online testing of each layer. Known methods are pyrometry, imaging (visible to near-infrared (NIR)), thermography (NIR to long-wavelength infrared (LWIR)) and interferometry [2], [4]–[6]. Previous work in this field has shown that LPBF parts embedded into powder can be tested with commercially available eddy current testing (ET) equipment [7]. After discovery of the giant magnetoresistance (GMR) effect [8], [9], GMR-based probes have proven that they are not only suitable for ET applications [10] but that they also outperform sensor coil-based systems in spatial resolution [11]. A single wire coil can be applied [12], [13] to precisely induce eddy currents. For easier signal conditioning of large GMR arrays, principles like multiplexing and heterodyning were implemented with discrete components or integrated into Application Specific Integrated Circuits (ASICs) ([14]–[18]. A probe design similar to the one in this paper, was used and compared to conventional coil based ECT in [17], [18] where an additional ASIC for signal conditioning was deployed. However, the discrete implementation

Manuscript received December 18, 2019; revised January 27, 2020; accepted February 6, 2020. This work was supported by the Bundesanstalt für Materialforschung und-prüfung within the focus area Materials. The associate editor coordinating the review of this article and approving it for publication was Prof. Boby George. *(Corresponding author: Henrik Ehlers.)*

Henrik Ehlers and Matthias Pelkner are with the Bundesanstalt für Materialforschung und-prüfung, 12205 Berlin, Germany (e-mail: henrik.ehlers@bam.de).

Roland Thewes is with the Sensor and Actuator Systems, Faculty of Electrical Engineering and Computer Science (EECS), Technical University of Berlin, 10623 Berlin, Germany.

Digital Object Identifier 10.1109/JSEN.2020.2973547

translates into a flexible, low cost solution thanks to its simplicity.

The testing width of those single wire probe designs can be expanded which makes it not only applicable in LPFB applications but also suitable for general ECT of wide flat surfaces where high testing rates are required. In this paper, these approaches are combined to set the basis for online ET of LPBF parts.

II. Methods

A. GMR Characteristics

The used GMR array is adapted for NDT applications and consists of 32 sensitive elements which are located near the edge of the chip.

Therefore, it can be positioned directly above the surface of the specimen to maximize the signal-to-noise-ratio (SNR).The pitch of 125 μm is suitable for detecting defects in this order of this magnitude [17]. The array as such was developed earlier within the framework of another project [17]. Transfer curve and frequency spectrum are measured using an OMICRON LAB Bode 100 vector network analyzer. To compare several elements of the whole array, four randomly chosen GMR elements are characterized.

Fig. 1 a) shows the characteristics of four GMR elements. The deviation of the slope in the linear region translates into a deviation in sensitivity between the elements. This does not only lead to variations of the nominal resistance value R_0 without any magnetic field but also to resistance differences in the saturation regions.

The transfer curve shows that the presence of a magnetic field leads to $\sim$ 6 % resistance change compared to R_0. The transfer curves reveal a linear region between roughly - 3 mT and + 5 mT. The linear region is approximated by the transfer function described through:

$$R_{H_Z} = S_{GMR} \cdot H_Z + R_0 \tag{1}$$

There, S_{GMR} is the sensitivity of the GMR element, R_0 its the nominal resistance, and H_z is magnetic field the device is exposed to. As an example, the transfer function of GMR1 is:

$$\Omega\Omega R_{H_Z} = 1.13\frac{\Omega}{\mathrm{mT}} \cdot H_Z + 168.50 \tag{2}$$

The frequency spectrum of the four GMR elements is shown in Fig. 1 b). The differences of the respective values R_0 are clearly visible. The spectra are flat up to the measured maximum frequency of 10 MHz.

B. Heterodyne Principle

The frequency of the excitation coil determines the penetration depth of the eddy currents into the material, and therefore also determines whether buried defects can be detected or only surface defect information is provided in the measurement signal. For this reason, the excitation frequency should be adjustable over a wide range (some kHz to some MHz). To fulfill the Nyquist theorem the sampling rate used for data acquisition must extend twice the maximum excitation frequency.

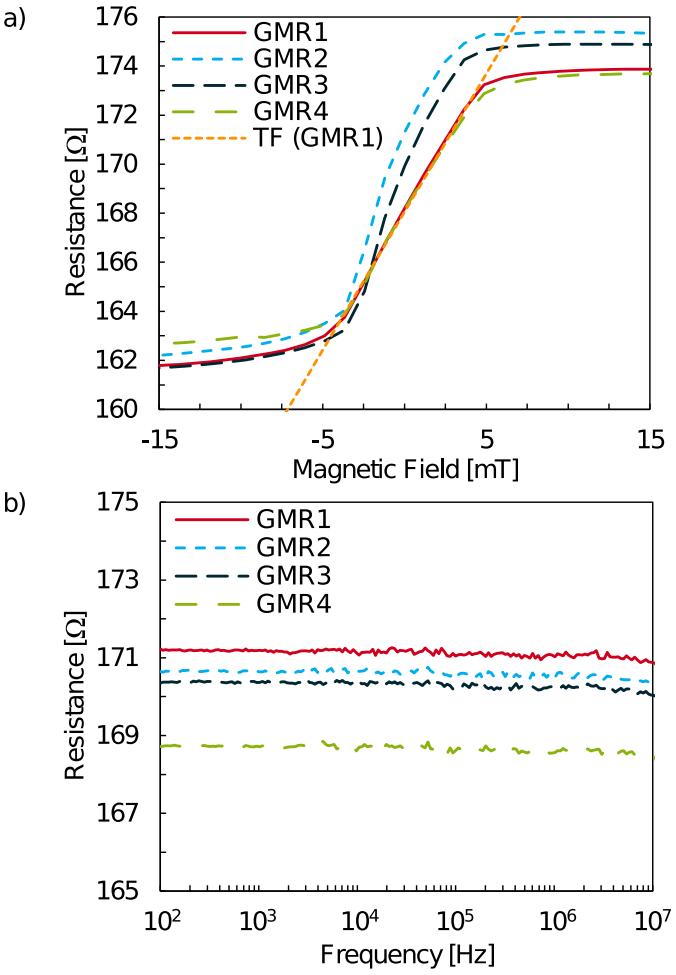

Fig. 1. a) GMR array characteristics for four randomly chosen GMR elements from a 32-element array and the approximated transfer curve (TF) within the linear region of GMR1 following (1). b) Frequency response of the four GMR elements without additional magnetic field.

Furthermore, the measured magnetic fields are in the order of a few μT [16] which leads to resistance changes of a few mΩ. Thus, ADCs providing high sampling rate and high resolution would be required. To keep the sampling rate as well as the influence of inductive coupling sufficiently low and to be robust against electromagnetic interference (EMI), a heterodyne principle is proposed in [14], [16]. Under condition that not only a current I_{coil} through the coil with frequency f_1 is applied but also an AC current I_{GMR} is forced through the GMR element with frequency f_2, heterodyne frequencies are formed containing the magnetic field information. One of these frequency components is of much lower frequency compared to both, f_1 and f_2, if these frequencies are adequately chosen and the following condition applies:

$$f_1 - f_2 \ll \frac{f_1 + f_2}{2} \tag{3}$$

To conserve phase information of the testing signal, generated frequencies f_1 and f_2 share a common reference clock. Heterodyning is achieved by using the circuit configuration depicted in Fig. 2. The GMR element R_{GMR} is operated in a Wheatstone bridge configuration with a potentiometer R_{Pot} for

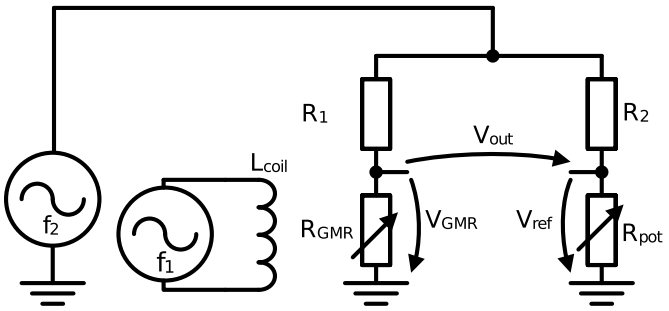

Fig. 2. Single GMR measurement using a Wheatstone bridge configuration with potentiometer R_{pot} for trimming, frequency generator with frequency f_1 for excitation coil current provision, and frequency generator with frequency f_2 for generating the bridge supply voltage to apply the heterodyne principle.

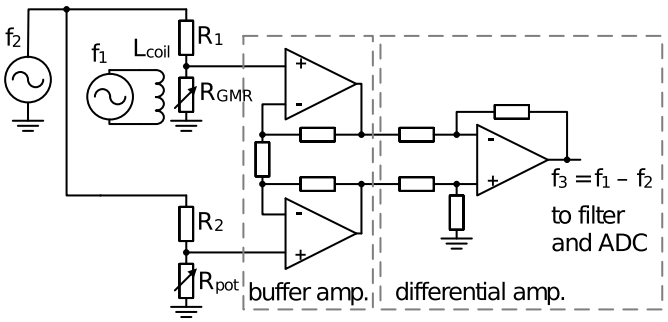

Fig. 3. Measurement circuit configuration using a heterodyne principle with a single GMR element in Wheatstone bridge configuration, a potentiometer for trimming in the opposite branch, a frequency generator with frequency f_1 for the excitation coil current, a frequency generator with frequency f_2 for generating the bridge supply voltage, and an instrumentation amplifier (consisting of buffer amplifiers and difference amplifier).

trimming. The excitation coil with inductance L_{coil} is driven with a sinusoidal current of frequency f_1. The Wheatstone bridge is operated with a sinusoidal voltage of frequency f_2, which results in a sinusoidal current I_{GMR} trough the GMR element.

Due to the sinusoidal current through L_{coil} the resistance of the GMR element R_{GMR} can be modeled by (4), with R_0 being the nominal resistance without external field, ω_1 being the angular frequency of the excitation and α being a fit parameter. The value of α depends on GMR sensitivity, distance from GMR and coil to the specimen coil current, and coil-to-GMR adjustment.

$$R_{GMR} = R_0 \left(1 + \alpha \cdot \cos\left(\omega_1 t\right)\right) \tag{4}$$

Considering the voltage divider configuration in both branches of the bridge, and with $\hat{V}_2$ being the amplitude of the bridge supply voltage with angular frequency ω_2, for voltages V_{GMR} and V_{ref} we achieve

$$V_{GMR} = \frac{R_{GMR}}{R_1 + R_{GMR}} \cdot \cos\left(\omega_2 t\right) \cdot \hat{V}_2 \tag{5}$$

and

$$V_{ref} = \frac{R_{Pot}}{R_2 + R_{Pot}} \cdot \cos\left(\omega_2 t\right) \cdot \hat{V}_2. \tag{6}$$

Using

$$R_1 = R_2 = R_{Pot} = R_0 \tag{7}$$

and (4), (5) can be written as:

$$V_{GMR} = \frac{R_0 \left(1 + \alpha \cdot \cos\left(\omega_1 t\right)\right)}{2 \cdot R_0 \left(1 + \frac{1}{2}\alpha \cdot \cos\left(\omega_1 t\right)\right)} \cdot \cos\left(\omega_2 t\right) \cdot \hat{V}_2. \tag{8}$$

Because of $|\alpha| \ll 1$, V_{GMR} can be approximated by:

$$\begin{aligned} V_{GMR} \approx{}& \frac{1}{2} \cdot \left(1 + \alpha \cdot \cos\left(\omega_1 t\right)\right) \\ & \cdot \left(1 - \frac{1}{2} \cdot \alpha \cdot \cos\left(\omega_1 t\right)\right) \\ & \cdot \cos\left(\omega_2 t\right) \cdot \hat{V}_2 \qquad (9) \\ \approx{}& \frac{1}{2} \cdot \cos\left(\omega_2 t\right) \cdot \hat{V}_2 + \frac{1}{4}\alpha \\ & \cdot \cos\left(\omega_1 t\right) \cdot \cos\left(\omega_2 t\right) \cdot \hat{V}_2. \qquad (10) \end{aligned}$$

By using an addition theorem, (10) can be re-written as:

$$\begin{aligned} V_{GMR} \approx{}& \frac{1}{2} \cdot \cos\left(\omega_2 t\right) \cdot \hat{V}_2 \\ & + \frac{1}{8}\alpha \left(\cos\left(\left(\omega_1 - \omega_2\right) t\right)\right. \\ & \left. - \cos\left(\left(\omega_1 + \omega_2\right) t\right)\right) \cdot \hat{V}_2. \end{aligned} \tag{11}$$

Equation (11) shows the effect of the heterodyning principle with two other frequency components being formed. One of these frequencies is ω_1 - ω_2, the other one equals $\omega_1 + \omega_2$. This implies that heterodyning in principle could be performed with only one half of the bridge. However, the large remaining portion of the biasing voltage in this case would minimize the usable dynamic range of the amplifier input. By using the difference voltage between V_{GMR} and V_{ref}

$$V_{diff} = V_{GMR} - V_{ref}, \tag{12}$$

calculating the difference of (6) and (11), and using (7), there are only heterodyne terms in the resulting voltage difference V_{diff}:

$$V_{diff} \approx \frac{1}{8}\alpha \cdot \left(\cos\left(\left(\omega_1 - \omega_2\right) t\right) - \cos\left(\left(\omega_1 + \omega_2\right) t\right)\right) \cdot \hat{V}_2. \tag{13}$$

This result is simplified in the sense that it does not consider inductive coupling into the GMR elements and traces due to the excitation coil. It also suggests the assumption that the bias voltage is fully canceled out. This is unfortunately not possible for all frequency ranges because the difference voltage is measured using an instrumentation amplifier consisting of two buffer amplifiers followed by a difference amplifier (Fig. 3). The buffer amplifiers with their high impedance inputs minimize the load on the bridge and the difference amplifier is cancelling out the bias voltage. The finite common mode rejection ratio (CMRR) leads to an imperfect cancellation for high frequencies and high bias voltages. The output voltage of the difference amplifier is then bandpass-filtered to separate the heterodyne frequency component.

To show that heterodyning is applicable the output spectrum of the instrumentation amplifier is measured. Data acquisition is performed using the spectrum analyzer module of a STEMlab 125-14 by Red Pitaya d.d (Solkan, Slovenia).

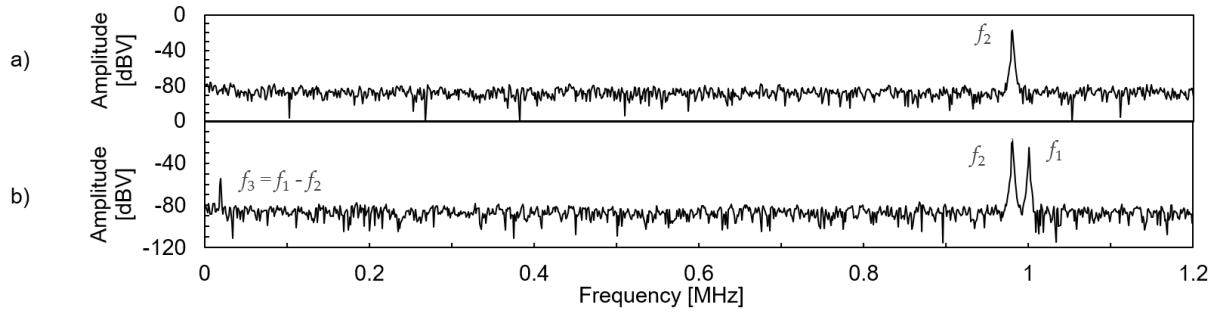

Fig. 4. Frequency spectrum of instrumentation amplifier output using a heterodyne principle a) without and b) with excitation at frequency f_1.

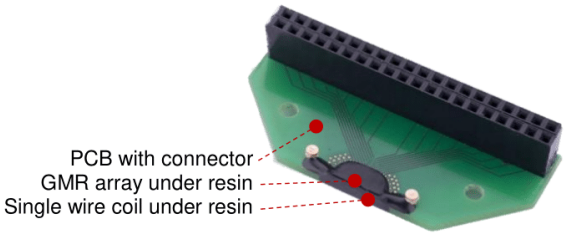

Fig. 5. GMR probe (Sensitec GmbH, Wetzlar (Germany)) with GMR array and a single wire coil under resin.

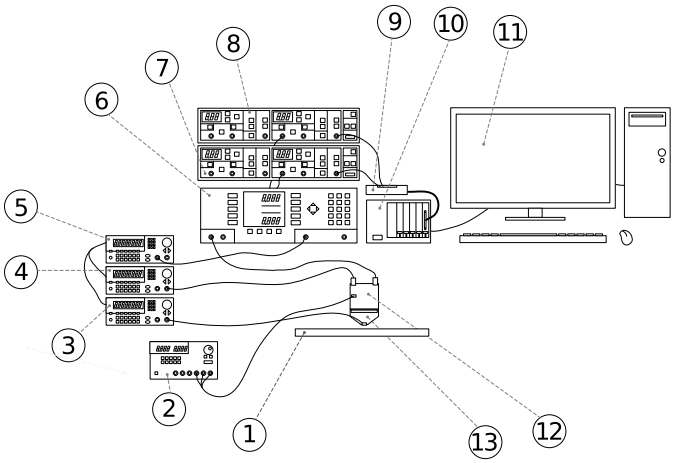

Fig. 6. Simplified sketch of the measurement setup. 1) Specimen, 2) power supply, 3) – 5) frequency generators, 6) lock-in amplifier, 7) and 8) filter, 9) i/o module, 10) DAQ System, 11) PC with software, 12) amplifier PCB, and 13) GMR probe, respectively.

The output spectrum of the difference amplifier without excitation is plotted in Fig. 4 a). The bias frequency f_2 is visible in the spectrum at 980 kHz due to the non-ideal behavior of the amplifier, i.e., the bias signal is not fully compensated. The effect of adding the excitation frequency f_1 at 1 MHz is shown in Fig. 4 b). A low frequency component $f_3 = f_1 - f_2$ is formed (together with a high frequency component $f_4 = f_1 + f_2$, which is not shown in this figure). In addition, the excitation frequency is present in this spectrum due to inductive coupling. A similar measurement is published in [16] with lower excitation and bias frequencies. When choosing a heterodyne frequency above 10 kHz, noise of the MR element is around 3 nV/$\sqrt{}$Hz [16], as required to measure magnetic fields in the μT range.

C. Measurement Setup and Test Samples

To detect defects in μm range, a sensitive ECT probe is necessary. To maximize the sensitivity, the distance between the GMR elements and specimen must be minimized. This was achieved by utilizing a GMR array with its sensitive elements close to the edge of the chip.

To precisely induce eddy currents while keeping distance between GMR Elements and specimen small, a single wire coil with a cross section of 125 μm by 20 μm is positioned in front of the array. Both, array and coil are coated with resin for protection. The GMR probe, shown in Fig. 5, is manufactured by Sensitec GmbH (Wetzlar, Germany). A comparable approach was used in [17], [18] where an additional ASIC for signal conditioning was deployed.

The measurement setup to utilize this GMR probe is shown in Fig. 6. Whereas future applications will utilize every element of entire arrays to achieve high spatial resolution at high testing speed and thus high throughput, here only a single GMR element is operated to investigate the feasibility of the method as such using the instrumentation amplifier configuration shown in Fig. 3.

The current in the single wire coil is driven by a frequency generator operated at frequency f_1. A second frequency generator providing f_2 is used to generate the bias voltage for the Wheatstone bridge. The output signal of the instrumentation amplifier is directly fed into a lock-in amplifier, whose reference frequency is generated by a third frequency generator which is set to $f_3 = f_1 - f_2$. The lock-in amplifier is utilized for I/Q demodulation. Two analog outputs containing X and Y information are filtered and connected to a data acquisition (DAQ) system. A scanning table (not shown) moves the probe along the surface of the specimen, and a PC controls the motion and the DAQ system.

To demonstrate that ET of a LPBF part is feasible, a mockup is prepared. A LPBF specimen entitled “316L-SLM-200” with artificial defects is printed utilizing 316L powder. The specimen is manufactured following a.STL file using an SLM 280 LPBF machine from SLM Solutions (Lübeck, Germany). The parameters used for manufacturing are listed in Table I.

The specimen contains 8 artificial surface defects and a marker for identification built into the part during the manu-

TABLE I
MANUFACTURING PARAMETERS FOR 316L-SLM-200 SPECIMEN WITH ARTIFICIAL SURFACE DEFECTS

Parameter	Value
layer height	50 µm
laser power	275 W
scan velocity	700 mm/s
hatch distance	120 µm
exposure strategy	meandering pattern (90° rotation every layer), contour scan
Powder	316L gas-atomized (10 – 45 µm)

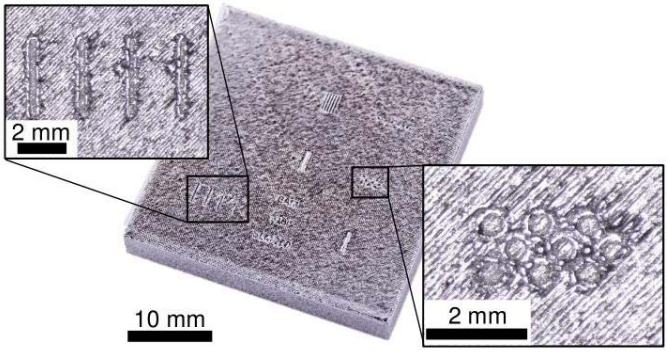

Fig. 7. LPBF specimen from 316L with artificial defects (316L-SLM-200).

facturing process. After manufacturing it is separated from the build plate using a saw. For improved testability the bottom is milled planar to the surface. The height of the specimen after post processing measures 5.6 mm. The finished part is displayed in Fig. 7. Two of its artificial defects are magnified. Due to the high surface and wall roughness, low defect depth and inaccuracies in geometry, precise defect dimensions cannot be extracted. However, notch widths between 100 μm and 200 μm and hole diameters of approximately 400 μm are estimated.

The specimen is adhered to a plastic frame filled with 316L powder to emulate powder influence. Fig. 8 shows the specimen embedded in a frame filled with powder together with the GMR probe and the amplifier PCB.

III. RESULTS

A. Heterodyning

The heterodyne principle is applied for the investigation of an aluminum test sample with artificial surface defects. The defects are five holes with a diameter of 440 μm and a depth of 250 μm, respectively. They are manufactured using Electrical Discharge Machining (EDM). A CAD drawing of the defects is shown in Fig. 9 a). The sample is tested using the GMR probe with a PCB-based instrumentation amplifier with a gain of 40 dB utilizing a single GMR element in scanning configuration. The coil current I_{coil} is set to 200 $\mathrm{mA_{pp}}$ at an excitation frequency of $f_1 = 1$ MHz. Two tests are performed. For the first (non-heterodyne) test the GMR current I_{GMR} is set to 5 mA DC. The ET data of this test are

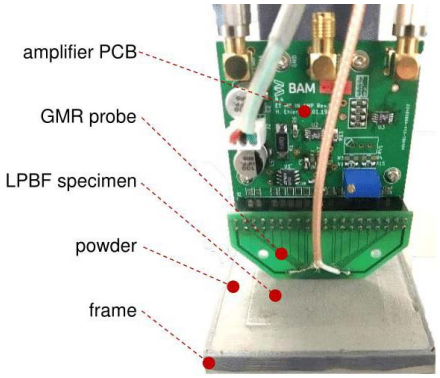

Fig. 8. Eddy current testing of LPBF specimen in 316L powder with artificial defects using GMR probe and amplifier PCB.

shown in Fig. 9 b) as a jet plot on the right and a line scan along the dashed line on the left. The second (heterodyne) test is performed applying a sinusoidal GMR current with an amplitude of 5 $\mathrm{mA_{pp}}$ and a frequency of $f_2 = 980$ kHz. The ET data are displayed in Fig. 9 c) as a jet plot on the right and a line scan along the dashed line on the left. The SNR is calculated using the RMS amplitude of the surface $V_{\mathrm{RMS,surface}}$ as reference value and the RMS amplitude of the defects $V_{\mathrm{RMS,defect}}$ along the 2D plot.

For both measurements, the single holes from the artificial defect structure can be resolved. The difference in phase angle found in Figs. 9 b) and c) originates from a difference of the phase angle of reference frequency f_3 to the phase angle of the excitation frequency f_1. Additionally, the SNR is reduced when applying the heterodyne principle because the magnetic field information is split into two components (f_1 - f_2 and f_1+ f_2). Nevertheless, heterodyning reduces the carrier frequency and therefore lowers the required sampling rate of the ADCs of the DAQ system. Thereby, the testing width can be economically scaled, which makes full build plate testing possible at all.

B. Powder

To verify that powder properties do not influence the measurement, the 316L-SLM-200 specimen is tested with and without powder. The measurement setup used is the same as shown in Figs. 6 and 8. For both tests, the heterodyning principle is applied. A coil current I_{coil} of 200 $\mathrm{mA_{pp}}$ is applied with an excitation frequency of $f_1 = 1.5$ MHz. The GMR current I_{GMR} is set to 5 $\mathrm{mA_{pp}}$ and a frequency of $f_2 = 1.48$ MHz resulting in a reference frequency of $f_3 = 20$ kHz for the lock-in amplifier. For the second test, powder is added to the frame. All other settings remain unchanged.

Fig. 10 b) shows the ET data with powder as a grayscale plot on the left and a line scan along the dashed line on the right. The dashed dotted box indicates the area of the plastic frame, that can be filled with powder.

Both sets of data are nearly identical, and any influence of powder is not observed. The contour of the specimen can clearly be distinguished from the surrounding area in both cases. The artificial surface defects are detected. Furthermore,

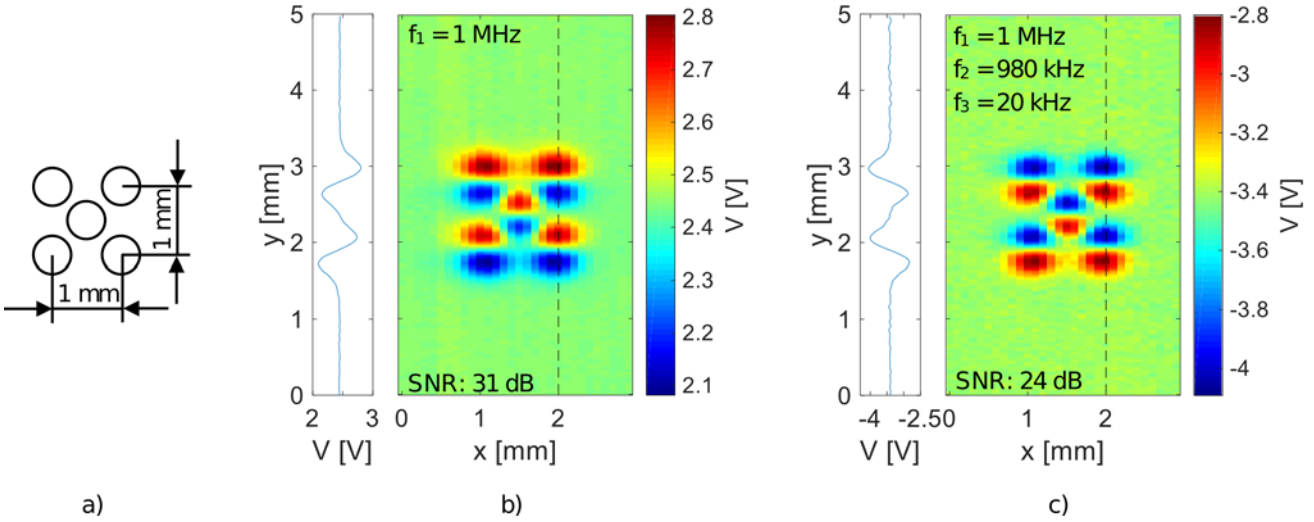

Fig. 9. a) CAD drawing of artificial defects in aluminum test sample. b) ET data of artificial defect in aluminum test sample without heterodyning. c) ET data of artificial defect in aluminum test sample with heterodyning.

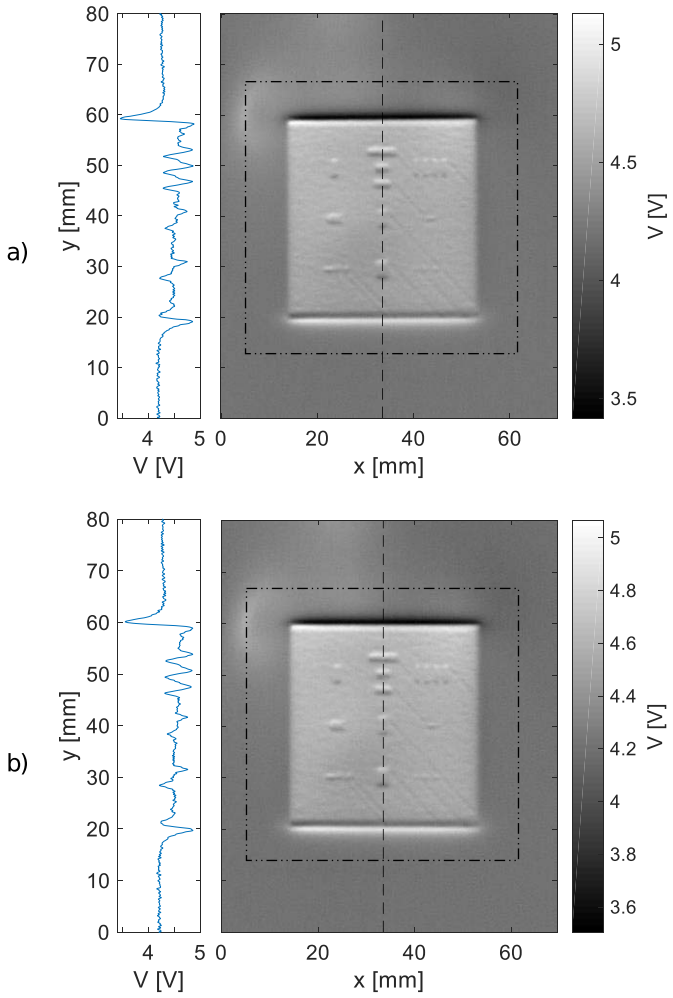

Fig. 10. ET data of 316L-SLM-200 printed part a) without and b) with powder (surrounding area that can be filled with powder is indicated by the dash-dotted line).

diagonal lines in the bottom right corner of the specimen are visible in both images. These lines result from surface non-homogeneities. They originate from the LPBF scanning strategy where two beam paths overlap.

C. Artificial Surface Defect

To evaluate how the GMR probe behaves in the case of small surface defects, one artificial surface defect of 316L-SLM-200 is investigated in more detail. The CAD drawing of the desired defect geometry is presented in Fig. 11 a). A microscopic picture of the artificial surface defect after manufacturing is shown in Fig. 11 b). The measurement setup used is the same as already introduced in Figs. 6 and 8.

Heterodyning is applied, coil and GMR currents, I_{coil} and I_{GMR}, of 200 $\mathrm{mA_{pp}}$ with excitation frequencies of $f_1 = 1$ MHz and $f_2 = 980$ kHz, respectively, are used resulting in a reference frequency of $f_3 = 20$ kHz for the lock-in amplifier. The ET data are plotted in Fig. 11 c) as a jet plot on the left and a line scan along the dashed line on the right.

The actual defect dimensions are not measured since proper depth and width information cannot be extracted due to roughness of specimen surface and walls of the notches. These non-homogeneities are visible in Fig. 11 b): they are related to small target geometries and the LPBF machine working at its resolution limits. A slight decrease in width from the bottom to the top notch is noticeable but the reduction is not as pronounced as in the CAD drawing (Fig. 11 a)). The data in Fig. 11 c) show that all four notches are detectable and a separation in space of the defects is possible. The notches slightly differ in width, which is also slightly visible in the data.

IV. Discussion

The measurements carried out in section II.A demonstrate that the applied GMR probes are suitable for ET with excitation frequencies of up to 10 MHz. With 1.13 Ω/mT the sensitivity S_{GMR} of the elements is sufficient. MR sensors based on other quantum mechanical effects like tunnel magnetoresistance (TMR) offer much higher sensitivities of up to

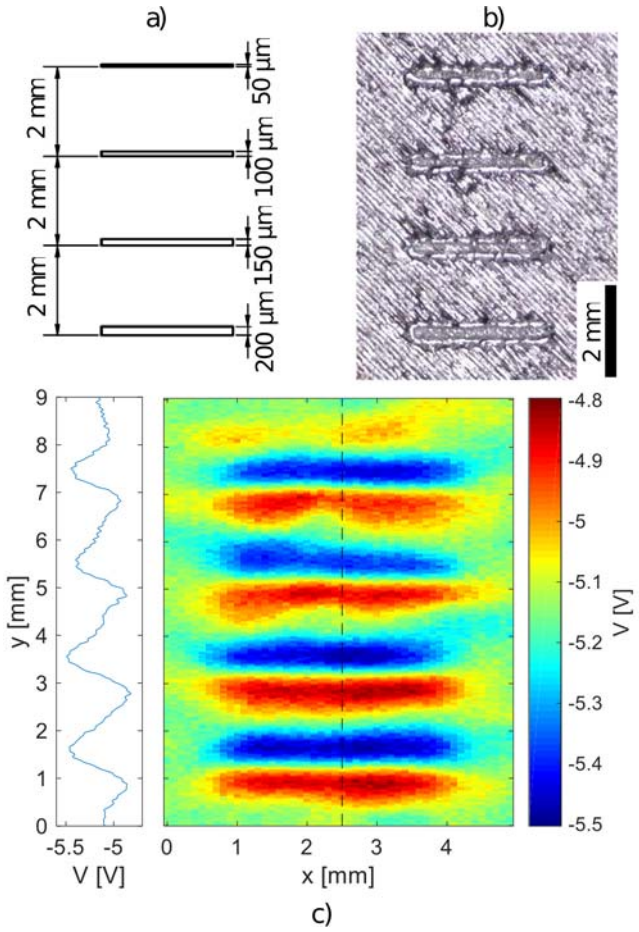

Fig. 11. a) CAD drawing of desired defect geometry (depth 200 μm). b) Microscopic picture of artificial surface defects in 316L-SLM-200 specimen. c) ET data of artificial surface defects in 316L-SLM-200 specimen.

$\sim$500 Ω/mT and a higher MR effect of up to $\sim$160% compared to their nominal resistance [18]. However, the higher noise [19] limits the accuracy and possible SNR of the whole ET system.

Furthermore, the heterodyne principle is not only a good signal conditioning method for decreasing the sampling rate of the data acquisition system by at least a factor of 50 but also enables reduction of the effect of inductive coupling induced by the excitation coil. Without heterodyning the expansion of the ET system to the whole LPBF build plate size is not economical. Although the SNR of the ET data with heterodyning obtained in section II.C is 26 dB, and, therefore, 7 dB lower than without, the artificial defect structures are detected.

Beyond that, embedding the 316L-SLM-200 specimen in 316L powder is an adequate method for simulated online testing of LPBF parts, although other environmental conditions like gas, pressure or temperature are not considered in this experiment. Nevertheless, the temperature will have an influence on the testing. During manufacturing of the LPBF sample the maximum measured temperature was around 100°C. At this temperature the conductivity of 316L is 13 % and the sensitivity of the probe 20% lower than at room temperature [20]. This results in an overall reduction of around 30 %.

However, feasibility is clearly demonstrated as the powder does not have an impact on the measurement results due to its much lower conductance. Furthermore, magnetic effects on powder are not observed during testing. Due to the single wire coil the magnetic field strength is too small to have any relevant physical effect on the powder. Both properties, i.e., not influencing the powder and not being influenced by it, combine to a key factor for online ET of LPBF parts.

Surface defects in the order of 100 μm can be detected. This makes this approach feasible for LPBF parts since defects sizes that occur during manufacturing are expected in the same order of magnitude. The results obtained in this paper are promising for online monitoring of LPBF. The geometry of the produced parts is visible and can be collected for each layer. Interestingly, not only artificial surface defects are detectable but also diagonal lines due to the laser scanning strategy. These artefacts are not deliberately manufactured but are clearly detected by the characterization method. The surface of the specimen and the background have the same noise level of roughly 100 mV_{pp}. Therefore, no difference due to higher surface roughness of the part is detected.

For enhanced information about the defect depth, Pulsed Eddy Current Testing (PECT) [21] may be considered. This, however, would increase complexity of the excitation signal generation and has not yet been considered in this work.

V. Conclusion

ET with MR sensors is a promising technique for the characterization of LPBF manufactured parts. The heterodyne principle minimizes metrology efforts while maintaining the defect information in comparison to conventional signal conditioning. Powder used in the LPBF process does not have any influence on ET and vice versa, which is an important fact for future online ET of LPBF parts. While testing a 316L test sample with artificial defects, it is shown that defects in the order of 100 μm can be detected.

In the future this approach will be extended towards online testing of each layer during the manufacturing process and combined with additional NDT methods for online monitoring of LPBF parts.

Although the first results show that the SNR decreases using the heterodyne approach, its reduced complexity, higher cost efficiency and the lack of inductive coupling from excitation wires, makes it a promising approach for future online monitoring of LPBF parts.

Acknowledgment

The authors would like to thank R. Pohl, A. Knöppchen, G. Mohr, and T. Heckel for supporting this work.

References

[1] W. Meiners, K. Wissenbach, and A. Gasser, "Shaped body especially prototype or replacement part production," DE Patent 19 649 865 C1, Feb. 19, 1998.

[2] M. Grasso and B. M. Colosimo, "Process defects and *in situ* monitoring methods in metal powder bed fusion: A review," *Meas. Sci. Technol.*, vol. 28, no. 4, Apr. 2017, Art. no. 044005.

[3] J. A. Cherry, H. M. Davies, S. Mehmood, N. P. Lavery, S. G. R. Brown, and J. Sienz, "Investigation into the effect of process parameters on microstructural and physical properties of 316L stainless steel parts by selective laser melting," *Int. J. Adv. Manuf. Technol.*, vol. 76, nos. 5–8, pp. 869–879, Feb. 2015.
[4] S. K. Everton, M. Hirsch, P. Stravroulakis, R. K. Leach, and A. T. Clare, "Review of *in-situ* process monitoring and *in-situ* metrology for metal additive manufacturing," *Mater. Des.*, vol. 95, pp. 431–445, Apr. 2016.
[5] Y. Chivel, M. France, and I. Smurov, "SLS-process monitoring and adaptive control," in *Proc. 4th Int. WLT–Conf. Lasers Manuf.*, Aug. 2015, pp. 1–7.
[6] J.-P. Kruth, J. Duflou, P. Mercelis, J. Van Vaerenbergh, T. Craeghs, and J. De Keuster, "On-line monitoring and process control in selective laser melting and laser cutting," in *Proc. 5th Lane Conf. Laser Assist. Net Shape Eng.*, vol. 1, no. 1, pp. 23–37, 2007.
[7] E. I. Todorov, "Non-destructive evaluation of additive manufacturing components using an eddy current array system and method," U.S. Patent 2016/034 921S A1, Dec. 1, 2016.
[8] G. Binasch, P. Grünberg, F. Saurenbach, and W. Zinn, "Enhanced magnetoresistance in layered magnetic structures with antiferromagnetic interlayer exchange," *Phys. Rev. B, Condens. Matter*, vol. 39, no. 7, pp. 4828–4830, Jul. 2002.
[9] M. N. Baibich *et al.*, "Giant Magnetorsistance of (001) Fe/(001) Cr magnetic superlattices," *Phys. Rev. Lett.*, vol. 61, no. 1, pp. 2472–2475, 1988.
[10] T. Dogaru and S. T. Smith, "Edge crack detection using a giant magnetoresistance based eddy current sensor," *Nondestruct. Test. Eval.*, vol. 16, no. 1, pp. 31–53, Jan. 2000.
[11] C. H. Smith, R. W. Schneider, T. Dogaru, and S. T. Smith, "Eddy current testing with GMR magnetic sensor arrays," *Rev. Prog. Quant. Nondestruct. Eval.*, vol. 2323, pp. 406–413, 2003.
[12] R. Hamia, C. Cordier, S. Saez, and C. Dolabdjian, "Eddy-current nondestructive testing using an improved GMR magnetometer and a single wire as inducer: A FEM performance analysis," *IEEE Trans. Magn.*, vol. 46, no. 10, pp. 3731–3737, Oct. 2010.
[13] J. Paul, C. Gebhardt, S. Raukopf, M. Kreutzbruck, A. Neubauer, and M. Pelkner, "Sensor arrangement for eddy-current testing of electrically conductive objects to be measured," WO Patent 2015/177 341 A1, Nov. 26, 2015.
[14] C. Fermon, M. Pannetier, N. Biziere, F. Vacher, and T. Sollier, "Method and device for non destructive evaluation of defects in a metallic object," U.S. Patent 2009/0 206 831 A1, Aug. 20, 2009.
[15] D. M. Caetano, M. Piedade, J. Graca, J. Fernandes, L. Rosado, and T. Costa, "Live demonstration: A CMOS ASIC for precise reading of a Magnetoresistive sensor array for NDT," in *Proc. IEEE Int. Symp. Circuits Syst. (ISCAS)*, May 2015, pp. 1–10.
[16] L. S. Rosado, F. A. Cardoso, S. Cardoso, P. M. Ramos, P. P. Freitas, and M. Piedade, "Eddy currents testing probe with magneto-resistive sensors and differential measurement," *Sens. Actuators A, Phys.*, vol. 212, pp. 58–67, Jun. 2014.
[17] M. Pelkner *et al.*, "Eddy current testing with high-spatial resolution probes using MR arrays as receiver," in *Proc. 7th Int. Symp. NDT Aerosp.*, 2015, pp. 1–8.
[18] D. M. Caetano *et al.*, "High-resolution nondestructive test probes based on magnetoresistive sensors," *IEEE Trans. Ind. Electron.*, vol. 66, no. 9, pp. 7326–7337, Sep. 2019.
[19] E. R. Nowak, R. D. Merithew, M. B. Weissman, I. Bloom, and S. S. P. Parkin, "Noise properties of ferromagnetic tunnel junctions," *J. Appl. Phys.*, vol. 84, no. 11, pp. 6195–6201, Dec. 1998.
[20] G. W. Anderson, Y. Huai, and M. Pakala, "Spin-valve thermal stability: The effect of different antiferromagnets," *J. Appl. Phys.*, vol. 87, no. 9, pp. 5726–5728, May 2000.
[21] G. Y. Tian, A. Sophian, D. Taylor, and J. Rudlin, "Multiple sensors on pulsed eddy-current detection for 3-D subsurface crack assessment," *IEEE Sensors J.*, vol. 5, no. 1, pp. 90–96, Feb. 2005.

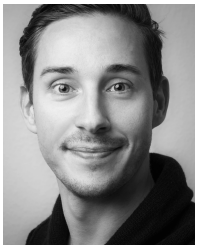

Henrik Ehlers received the master's degree in mechatronics from the Beuth University of Applied Sciences Berlin (BHT), Berlin, Germany, in 2014. He is currently pursuing the Ph.D. degree with the Technical University of Berlin, Berlin.

From 2014 to 2018, he worked as a Hardware Design Engineer in the fields of high-power laser diode drivers and SoC-based industrial vision at Scansonic MI GmbH, Berlin. Since 2015, he has held many lectures regarding basics of mechatronics and electrical components at BHT. Since 2018, he has been with the Federal Institute for Materials Testing and Research (BAM), Berlin. He has specialized in eddy current testing for additive manufacturing, which is also his Ph.D. topic.

Matthias Pelkner received the degree in physics from the Technical University of Munich, the Diploma degree in 2008, and the Ph.D. degree in 2014. He specialized in semiconductor physics and magnetism. Afterward, he has started to work with the Federal Institute for Materials Testing and Research (BAM), Berlin, Germany, in 2009. Since 2014, he has been part of the Division 8.4 Acoustic and Electromagnetic Methods, Eddy Current Testing Group. He is responsible for electromagnetic testing and magnetic material characterization. His research work interests include sensor development, simulation, and data analysis for electromagnetic non-destructive evaluation.

Roland Thewes (Senior Member, IEEE) received the Dipl.Ing. and Dr. Ing. degrees in electrical engineering from the University of Dortmund, Dortmund, Germany, in 1990 and 1995, respectively.

In 1994, he joined Research Laboratories, Siemens AG, where he was active in the design of nonvolatile memories and in the field of reliability and yield of analog CMOS circuits. From 1997 to 1999, he managed projects in the fields of design for manufacturability, reliability, analog device performance, and analog CMOS circuit design. From 2000 to 2005, he was responsible for the Lab on Mixed-Signal Circuits of Corporate Research of Infineon Technologies focusing on CMOS-based bio-sensors, low-voltage analog CMOS circuit design, and device-circuit interaction. From 2006 until March 2009, he was heading the department focusing on advanced DRAM core circuitry in the Product Development Division, Qimonda. Since April 2009, he has been a Professor with the Technical University of Berlin (TU Berlin), Berlin, Germany, focusing on CMOS-based sensor systems. He has authored or coauthored more than 160 peer-reviewed technical publications and authored or coauthored a similar number of granted patents and patent applications.

Dr. Thewes has served as an Elected Member for the IEEE SSCS AdCom. He is a member of the German Association of Electrical Engineers and the German Academy of Science and Engineering. He was a recipient of the German President's Future Award in 2004, the ISSCC 2002 Jack Raper Award in 2003, and a recipient or co-recipient of eight further paper and conference awards. He has been serving on the Technical Program Committees for various conferences, among these the IEEE IEDM, the IEEE ISSCC, the IEEE ESSCIRC, and the IEEE BioCAS.